

---

## Detection of iceberg using Delay Doppler and interferometric Cryosat-2 altimeter data

Tournadre Jean <sup>1,\*</sup>, Bouhier Nicolas <sup>4</sup>, Boy F. <sup>2</sup>, Dinardo S. <sup>3</sup>

<sup>1</sup> Laboratoire d'Océanographie Physique et Spatiale, IFREMER, CNRS, Université de Bretagne Occidentale, Plouzané, France

<sup>2</sup> Centre National d'Etudes Spatiale, Toulouse, France

<sup>3</sup> HeSpace/EUMETSAT, Darmstadt, Germany

<sup>4</sup> FRANCE

\* Corresponding author : Jean Tournadre, email address : [jean.tournadre@ifremer.fr](mailto:jean.tournadre@ifremer.fr)

---

### Abstract :

The Cryosat-2 Synthetic Aperture Interferometric Radar Altimeter (SIRAL) altimeter is the first altimeter that can operate in three different modes over the ocean: the classical pulse limited LRM, the Delay Doppler or SAR and the SAR Interferometric modes. It offers a unique opportunity to test, validate and compare the capabilities of the three modes for the detection and analysis of small icebergs (<3 km in length) already demonstrated for classical altimeters. Over most of the sea-ice free ocean, SIRAL operates in LRM mode and the classical iceberg detection algorithm can be applied without modification. It can also be applied to the Reduced SAR or pseudo-LRM data computed from SAR and SARin data. In SAR mode, iceberg signatures are bright spots in the waveform thermal noise part. They can be easily detected using classical image processing tools. The area of the iceberg is estimated using the size of the signature. In SARin mode, the coherence of the signals can insure the presence of scatterers above the sea surface and is used with the SAR detection algorithm to reduce the probability of false alarm and to better delineate icebergs. Interferometry allows for the first time to map the iceberg and the iceberg free-board at an unprecedented resolution opening a new way of investigation of the distributions of size, free-board and volume of the small icebergs that are responsible of large fraction of the freshwater flux into the ocean.

### Highlights

► Detection of small icebergs using Cryosat-2 altimeter 3 modes (LRM, SAR, SARin) ► Estimation of iceberg's area from the three modes ► First method of estimation of iceberg freeboard from Interferometric altimeter data

**Keywords :** Small iceberg detection using Cryosat-2 three modes of operation, Estimation of iceberg's area, Estimation of iceberg's free-board from Interferometric altimeter data

## 1 **1. Introduction**

2 Icebergs are an important part of the climate system as they interact  
3 with the ocean, atmosphere and cryosphere (Hemming, 2004; Smith, 2011).  
4 They represent up to half of the mass loss of Antarctic ice sheet (Rignot  
5 et al., 2013; Depoorter et al., 2013) and play an important role in the global  
6 freshwater cycle by delivering freshwater to regions far from the ice sheet  
7 margins (Tournadre et al., 2016; Gladstone et al., 2001; Silva et al., 2006). In  
8 the northern hemisphere, ice discharge from the Greenland Ice sheet increased  
9 between 2000 and 2012 while its relative contribution to the total volume loss  
10 declined from 58% before 2005 to 32% between 2009 and 2012 (Enderlin et al.,  
11 2014). The iceberg cold melt-water affects the upper ocean by freshening  
12 and cooling due to their uptake of latent heat. Several studies have revealed  
13 that freshening and cooling have opposing effects on ocean stratification,  
14 as cooling enhances the surface density, promoting deep mixing, whereas  
15 freshening decreases the water density, stabilizing the water column (Jongma  
16 et al., 2009; Green et al., 2011). Numerical models of the Southern Ocean

17 circulation are now routinely interactively coupled with a thermodynamic  
18 iceberg model (Jongma et al., 2009; Merino et al., 2016).

19 In the Southern Ocean, large icebergs ( $>400 \text{ km}^2$ ) transport over 70% of  
20 the volume of ice but their melting only represents 20% of the total mass loss  
21 (Tournadre et al., 2016). Small icebergs ( $<10 \text{ km}^2$ ), although they constitute  
22 only 3-5% of the total ice volume, represent the major part of the freshwater  
23 flux into the ocean (Tournadre et al., 2016). While large icebergs transport  
24 ice over long periods and large distances they constantly generate smaller  
25 icebergs through fragmentation, the latter acts as a diffusive process and are  
26 the main component of the freshwater flux (Tournadre et al., 2016).

27 Tournadre et al. (2008) demonstrated that icebergs between 0.01 and  
28  $9 \text{ km}^2$  (0.1 to 3 km in length for square icebergs), referred as small icebergs  
29 thereafter, at least in open water, have a detectable signature in the ther-  
30 mal noise part (TNP) (i.e. above the sea surface) of high resolution (HR)  
31 waveforms of pulse-limited altimeters that can be easily detected. Under  
32 hypotheses of constant ice backscatter and iceberg free-board, the iceberg's  
33 area can be inferred from the measured backscatter and range (Tournadre  
34 et al., 2012). A twenty-two year (1992-2014) Southern Ocean climatology of  
35 the probability of presence, volume of ice and surface based on the analy-  
36 sis of the archives of nine conventional altimeters has been produced within  
37 the french Centre National d'Etudes Spatiales founded ALTIBERG project  
38 (Tournadre et al., 2016). Synthetic Aperture Radar (SAR) imagers are also  
39 powerful instruments to detect, analyze and characterize iceberg. Several ice-  
40 berg detection algorithms have been published based on single channel data  
41 (Gill, 2001; Gladstone and Bigg, 2002; Silva and Bigg, 2005; Wesche and

42 Dierking, 2012; Mazur et al., 2017a) or more recently on fully-polarimetric  
43 SAR data (Denbina and Collins, 2014; Marino et al., 2016). SAR imagers are  
44 well designed to study the spatial distribution of icebergs, but, mainly be-  
45 cause of the irregular and poor coverage of some regions (such as the South  
46 Atlantic), it is not yet possible to build a small iceberg climatology using  
47 SAR data. Furthermore, the amount of data to process and the computing  
48 time required by the SAR detection algorithms, even with the increase of  
49 computer processing capabilities, still limit their operational use. On an-  
50 other hand, the limited swath of altimeters while limiting their capability  
51 to estimate an instantaneous spatial distribution, allows to obtain indepen-  
52 dent random samples of the iceberg population. This, combined with their  
53 regular temporal sampling patterns, allows a good estimate of the statistical  
54 characteristics of the iceberg ensemble (probability of presence, area).

55 Since the launch of Cryosat-2 in 2010, a new generation of altimeters using  
56 Doppler and interferometric capabilities has emerged and will most probably  
57 become the standard for the upcoming altimeters, at least the Doppler one  
58 as it is already the case for the Sentinel-3 altimeter launched in 2016 (Wing-  
59 ham et al., 2006). The Delay-Doppler Altimeter (DDA) concept (also known  
60 as SAR altimetry) was first proposed by Raney (1998). Delay-Doppler al-  
61 timeters have high pulse repetition frequency (PRF) to ensure pulse-to-pulse  
62 coherence, leading to a potential along-track resolution around 300 meters,  
63 improved signal-to-noise ratio and enhanced altimeter ranging performance.  
64 The Cryosat-2 Synthetic Aperture Interferometric Radar Altimeter (SIRAL)  
65 uses the SAR mode over ocean areas where sea ice is prevalent as well as  
66 over some test areas (ESA-ESTEC, 2007).

67 The SAR interferometric mode (SARin) is CryoSat's most advanced mode,  
68 primary used around the ice sheet margins and over mountain glaciers. Here,  
69 the altimeter performs synthetic aperture processing and uses a second an-  
70 tenna as an interferometer to determine the across-track angle to the earliest  
71 radar returns. The SARin mode provides thus the exact surface location  
72 being measured when the surface is sloping and can be used to study more  
73 contrasted terrains, like the margins of the Antarctic continent or Green-  
74 land. Over most of the sea-ice free ocean, SIRAL operates in the standard  
75 Low Rate Mode (LRM) that is the conventional pulse-limited radar altimeter  
76 mode. In this mode the data rate is much lower than for the other measure-  
77 ment modes. The SIRAL data offer a very good opportunity to test the  
78 capabilities and merits of three different altimeter operating modes for the  
79 detection and estimation of small icebergs characteristics (free-board and  
80 surface). The algorithms that will be developed will then be used in the near  
81 future to process the whole archive of Cryosat-2 and Sentinel-3 to increase  
82 the existing ALTIBERG database. They will also be used to improve our  
83 knowledge of the geographical distribution of small icebergs (especially in  
84 the Northern Hemisphere), their distribution of size and the volume of ice  
85 they transport. Finally, they will be included in the operational processing  
86 chains of future SAR and SARin altimeters.

87 The data, detection method and quantification of iceberg characteristics  
88 for the three operating modes are presented in Section 2. For SAR and SARin  
89 modes, a case study comparing the results of the altimeter data analysis to  
90 cloud free satellite visible or SAR images is presented. It is always quite  
91 difficult to find clear visible images coincident with altimeter passes and

92 SAR images were, until the launch of Sentinel-1A which provides a much  
93 better coverage of high latitude regions, quite scarce. The two best cases we  
94 found are located near Greenland and demonstrate thus that the detection  
95 is also possible in the Northern Hemisphere where icebergs are generally  
96 smaller than Southern Ocean ones. The SAR and SARin mode are also  
97 compared to the Reduced SAR mode, i.e. to pseudo-LRM (pulse limited like)  
98 data computed from SAR or SARin data through a process known as SAR  
99 reduction (Boy et al., 2016; Gommenginger et al., 2013). Indeed, in order  
100 to build long time series of iceberg statistics it is essential to have a base of  
101 inter-comparison and inter-calibration between pulse limited altimeters and  
102 SAR-SARin ones.

## 103 **2. CRYOSAT-2 SIRAL data and Method of detection**

104 CryoSat-2 orbits on a non-sun-synchronous polar orbit ( $92^\circ$  inclination)  
105 at an altitude of 713 km. A detailed description of the mission and altimeter  
106 is given by Wingham et al. (2006) and an overview of the products in ESA-  
107 ESTEC (2007). The default SIRAL operating modes, LRM, SAR, SARin or  
108 no measurement, are determined using a geographical mask defined by the  
109 satellite mission control center. The mean coverage of the different modes is  
110 given in Figure 1.

### 111 *2.1. LRM detection*

112 In LRM mode, SIRAL operates in the classical pulse limited mode. The  
113 Tournadre et al. (2008) method of iceberg detection that has already been  
114 applied to eight altimeters by Tournadre et al. (2016) to create the AL-  
115 TIBERG small icebergs database can be applied without modification to the

116 Cryosat-LRM data. Basically, any target emerging from the sea surface gives  
117 an echo in the TNP of altimeter waveforms if its range lies within the altimeter  
118 analysis window and if its backscatter is higher than the noise level. The  
119 range depends on the distance from nadir and on the target elevation. The  
120 target signature in the waveform space is a parabola whose characteristics  
121 depend only on the orbit parameters. The method of detection is presented  
122 in detail by Tournadre et al. (2008) and is summarized in Appendix. The  
123 Cryosat-2 LRM archive has already been processed and is included within  
124 the ALTIBERG data set (Tournadre et al., 2016). Figure 2 presents all the  
125 icebergs detected in the Southern Ocean from 2010 to 2016 as well as an ex-  
126 ample of detected iceberg signatures. The iceberg area is estimated from the  
127 iceberg backscatter and range using a backscatter model (Tournadre et al.,  
128 2012, 2016).

129 While it is not possible to transform LRM mode to SAR mode data, it  
130 is possible to generate pseudo-LRM data from SAR or SARin data through  
131 a process known as SAR reduction or RDSAR. Several methods have been  
132 proposed to produce pseudo-LRM (RDSAR) by Boy et al. (2016) or Gom-  
133 menginger et al. (2013). It is beyond the scope of this paper to analyze  
134 the different RDSAR methods that give very similar results for the wave-  
135 form TNP where iceberg signatures can be detected. The LRM detection  
136 algorithm can also be applied to RDSAR data without modifications. An  
137 example of iceberg signature in RDSAR data is given in Figure 4-a and -b.

## 138 *2.2. Delay Doppler or SAR Mode*

139 The SAR mode is used over ocean areas where sea ice is prevalent and  
140 over some test areas. In this mode, the altimeter transmits bursts with a

141 frequency of about 85 Hz (Wingham et al., 2006). Each burst contains 64  
142 coherent pulses (transmitted at a 18,182 Hz PRF) which are measured over  
143 time windows of 128 bin length (60 m) and are then processed by along-  
144 track FFT to obtain the Delay Doppler map (DDM) of the surface-reflected  
145 signal. Sixty-four Doppler beams of equal angular sectors are thus obtained.  
146 Each Doppler beam is about 250 m wide in the along-track direction and  
147 the interval between bursts corresponds to the satellite moving forward by  
148 80 m each time in SAR mode (290 m in SARin mode). The strips laid down  
149 by successive bursts can be “stacked” to obtain multiple looks of the same  
150 portion of the surface. After range alignment including slant, tracker and  
151 Doppler range corrections and after range compression (Dinardo, 2013; Ray  
152 et al., 2015; Boy et al., 2016), stacks of co-located Doppler beams (L1B-S  
153 data) are produced. The incoherent summation of the L1b-S finally gives  
154 the SAR Echo (or waveform). In this study, we used the DDM from the  
155 ESA Level-1A (FBR) data and the SAR waveforms from the ESA Level-1B  
156 data. The L1B-Ss were obtained using the ESA Grid Processing On-Demand  
157 (GPOD) and SARvatore (SAR versatile altimetric tool-kit for ocean research  
158 and exploitation) (Dinardo, 2013) that allows to reprocess Level-1A data  
159 using the user’s own configuration parameters.

160 Figure 4 presents an example of iceberg detection using SAR mode data  
161 near Greenland (see Figure 3). Two icebergs are clearly visible on the MODIS  
162 image taken 5 hours before the Cryosat pass 2889 cycle 9, on 07/10/2015.  
163 The iceberg signatures are clearly visible in the RDSAR waveforms near  $74.9^\circ$   
164 N and  $75.0^\circ$  N in the form of characteristic parabolas similar to the ones  
165 presented in Figure 2. The waveforms have been re-positioned using the L1

166 window delay provided by the initial height or a coarse height and fine height  
167 (Bouzinac, 2012). The detection of the two icebergs using RDSAR data is  
168 illustrated in Figure 4-a and b. The convolution of the waveforms and the  
169 parabolic filter characteristic of iceberg signature (Figure 4-b) is first used  
170 to detect the local maximums of correlation (red isolines) and the waveforms  
171 are then used to estimate the position and value of maximum backscatter  
172 represented as black circles in Figure 4-a. Two less intense parabolas associ-  
173 ated to the iceberg’s signatures can also be seen at  $74.9^\circ$  N and  $75.0^\circ$  N. They  
174 correspond to echoes from scatterers at different elevations and/or locations  
175 within the iceberg. By design the LRM detector detects only the strongest  
176 echo.

177 Figure 4-e and -f present the DDM and L1b-S echoes at  $75^\circ$  N, i.e where  
178 the northernmost iceberg is closest to the ground track. Within the DDM  
179 the iceberg’s signature reduces to a bright spot within the waveform TNP.  
180 Its range depends on the iceberg’s free-board and distance from nadir while  
181 its Doppler frequency depends of the along-track distance. The stacking and  
182 multi-looking process corrects the range within the DDM and co-locates the  
183 Doppler beams from different bursts. The iceberg’s signature within L1b-S  
184 should therefore be a bright line of constant range (Figure 4-d). However,  
185 the specularity of ice backscatter and the antenna beam pattern limit the  
186 signature to small incidences.

187 The incoherent summation used to produce the SAR echoes reduces the  
188 icebergs LRM/RDSAR parabolic signatures to bright spots (Figure 4-c).  
189 This kind of signatures was also observed for ships (Gómez-Enri et al., 2016).  
190 Several image processing algorithms exist to detect bright spots. They are

191 based on noise reduction, signal enhancement and signal thresholding to cre-  
 192 ate a binary image in which connected components (CC) are detected (see  
 193 for example Smal et al. (2010)).

194 Compared to LRM/RDSAR data, the L1B-S incoherent summation also  
 195 strongly reduces the noise level of the waveforms TNP used for detection. It  
 196 can be considered as negligible, which facilitates the detection. To enhance  
 197 the iceberg signatures, the waveforms are normalized by the mean waveform  
 198 ( $\overline{WF}$ ) and rms ( $\sigma_{WF}$ ) computed for each Cryosat cycle,

$$199 \quad WF'(i, j) = (WF(i, j) - \overline{WF}(j)) / \sigma_{WF}(j) \quad (1)$$

200 A binary image is then created by thresholding  $WF'$  at 4 (i.e.  $4\sigma_{WF}$ ). The  
 201 image CC's are computed using a classical graph theory algorithm such as the  
 202 Matlab© *bwconncomp* or SCiPy *label* routines. The CC's properties; area,  
 203 position, mean and max backscatter; are then estimated using Matlab© or  
 204 SCiPy *regionprops* routines. The icebergs detected using this algorithm are  
 205 shown as red isolines in Figure 4-c. Table 1 presents the iceberg's characteris-  
 206 tics in RDSAR and SAR data. The two main icebergs signatures in RDSAR  
 207 data are also detected at the same locations in SAR data (number 1 and 4  
 208 in Table 1). The iceberg SAR maximum backscatter is significantly smaller  
 209 than the RDSAR ones (Table 1) because the L1b-S averaging while reducing  
 210 the noise level also smooths the iceberg signatures because of the high ice  
 211 specularity compared to water.

212 The SAR algorithm allows the detection of the secondary signatures of the  
 213 two icebergs (number 2 and 3) as well as the detection of an iceberg (number  
 214 5) too small to be detected in the MODIS image and whose backscatter is  
 215 not high enough to come out of RDSAR noise. The area of the two main

216 icebergs is estimated at 1.1 and 0.26 km<sup>2</sup> using the RDSAR backscatter and  
 217 the Tournadre et al. (2016) method. Due to the low resolution of MODIS  
 218 images (250 m) and the difficulty of precisely delineate the icebergs only crude  
 219 area estimates can be made. The image analysis gives 0.6-1 km<sup>2</sup> and 0.3-0.4  
 220 km<sup>2</sup> for the two icebergs; in good agreement with the RDSAR values. The  
 221 icebergs area can also be estimated from the size of SAR signature. While  
 222 the along-track resolution is 300 m, the across-track resolution depends on  
 223 free-board elevation and distance from nadir (Equation A.1). Icebergs with  
 224 28 m free-boards can only be detected if their distance from nadir ranges  
 225 from 2 to 7 km (Tournadre et al., 2016). Between 2 and 7 km, the SAR  
 226 range bin width,  $dy$ , varies from  $\sim 75$  to  $\sim 20$  m. Two area estimates are  
 227 computed, the first one is the sum of the CC's area multiplied by the along  
 228 track and across-track resolution

$$229 \quad a_i = \sum_j s_j dx dy \quad (2)$$

230 where  $s_i$  are the area (in pixels) of the CCs associated to the iceberg,  
 231 and  $dx$  and  $dy$  are along and across-track resolutions. The second method  
 232 assumes that the iceberg's length in range,  $l_y$ , extends from the minimum  
 233 to the maximum range values of the CC's detected at the same along-track  
 234 location while the width,  $w_x$ , is the along-track width. The iceberg's area is  
 235 thus

$$236 \quad A_i = w_x dx l_y dy \quad (3)$$

237 The minimum and maximum of range bin width,  $dy$  are then used to  
 238 compute minimum and maximum values of the two area estimates. The first

Table 1: Characteristics of the detected icebergs in Cryosat-2 SAR pass 2889 cycle 9, 2015/10/07 23:36 UT; RCS: radar cross section

	SAR							RDSAR			
	Lat	Range		Area		Mean	Max	Lat	Range	RCS	Area
				Method1	Method2	RCS	RCS				
	deg	bin	pixel	km <sup>2</sup>	km <sup>2</sup>	dB	dB	deg	bin	dB	km <sup>2</sup>
1	75.006	18	11	0.20-0.48	0.45-1.05	-11.2	-9.7	75.006	34	4.2	1.1
2	75.006	35	12			-2.4	2.2				
3	74.913	30	14	0.16-0.38	0.30-0.71	-9.6	-7.0	74.913	41	2.6	0.3
4	74.913	42	4			-3.1	-2.1				
5	74.900	10	3	0.03-0.06	0.03-0.06	-14.2	-13.8				

239 method gives 0.2-0.48 and 0.16-0.38 km<sup>2</sup> for the two icebergs while the sec-  
240 ond ones gives 0.45-1.05 and 0.30-0.71 km<sup>2</sup> respectively. Compared to the  
241 RDSAR and MODIS estimates, the first method appears to largely under-  
242 estimate the area (by almost a factor 2) while the second method estimates  
243 are of the same order of magnitude (see Table 1). The sensitivity of the  
244 detection and size estimate on the power threshold is presented in Appendix  
245 Appendix B.

246 The uncertainty on range bin size, as well as the difficulty to precisely  
247 estimate the size of the signature lead to a large uncertainty on the SAR  
248 area estimate. RDSAR area estimates are certainly more robust. It should  
249 be noted that the new Sentinel-3 L1 products provided both RDSAR and  
250 SAR echoes and can be used to better analyzed the relationship between  
251 backscatter, signature size and icebergs area. For the smaller iceberg detected

252 at 74.9° N, the area can only be estimated using SAR data and both methods  
253 give an area of 0.03-0.06 km<sup>2</sup>.

### 254 *2.3. SAR interferometry mode*

255 The principles of interferometric altimetry were first proposed by Jensen  
256 (1999) and lead to the development of the Cryosat mission. A detailed de-  
257 scription of the principles and processing of the Cryosat SARin data is given  
258 in Wingham et al. (2006). The main (left) antenna transmits the radar signal  
259 and the two antennas measure the backscattered echo waveform (see Figure  
260 5). The main complex waveform is multiplied with the complex conjugate  
261 of the second antenna waveform. The phase of the resulting cross-channel  
262 waveform is then defined as the interferometric phase difference, which results  
263 from the slight range difference of an off-nadir scatterer for the two antennas.  
264 The normalized modulus of the conjugate product gives the estimate of the  
265 signal coherence. The stacked SAR echoes for both antennas are computed  
266 using the SAR mode processing. The SAR echoes, phase and coherence are  
267 provided in ESA Level-1B products. In SARin mode the waveform analysis  
268 window is increased to 512 bins (240 m) to better sample sloping terrains.  
269 In the Baseline-C data products used in this study, the use of zero-padding  
270 prior to FFT processing further increase the number of range bins to 1024  
271 without changing the range window. Each bin corresponds thus to 1.565 ns  
272 or 0.23 m in range.

273 The interferometric phase difference,  $\Delta\psi$ , is related to the off-nadir angle,  
274  $\alpha$ , by

$$275 \quad \Delta\Psi = \frac{2\pi B}{\lambda} \sin(\alpha) \quad (4)$$

276 where  $\lambda$  is the radar wavelength and  $B$  is interferometer baseline (distance  
 277 between the two antennas). Under the small angle approximation, the off-  
 278 nadir angle  $\alpha$  is

$$279 \quad \alpha = \frac{\lambda \Delta \Psi}{2\pi B} \quad (5)$$

280 Galin et al. (2013) estimated an angle scaling factor  $a$  ( $\alpha' = \alpha/a$ ) to compen-  
 281 sate slight differences between the two SIRAL antennas. The across-track  
 282 distance to nadir,  $d_0$ , is given

$$283 \quad d_0 = H_i \alpha' \quad (6)$$

284 where  $H_i$  is the range defined by  $H_i = ct_i/2$ ,  $t_i$  being the pulse two-way travel  
 285 time.

286 Taking the earth's curvature into account, an iceberg detected in range  
 287 bin  $b_1$ , corresponding to travel time  $t_1$ , and at off-nadir  $\alpha_1$ , has a free-board  
 288 given by (Nanda, 2015)

$$289 \quad \delta = (H - H_i \cos \alpha_1 + R_E (1 - \cos \beta)) \cos \beta \quad (7)$$

290 where  $\beta = H/R_E \alpha_1$  and  $H_i = ct_1/2$ . The SARin echoes are similar  
 291 to the SAR ones, except that the number of range bins in the echoes TNP  
 292 is significantly larger (125x2 vs 50). The swath over which icebergs can be  
 293 detected which is of the order of 6 km is thus significantly increased to 12  
 294 km. The SAR detection algorithm can be applied to the SARin waveforms  
 295 without modification. However, in the echoes TNP the signals received by  
 296 the two antennas are by nature random noise and thus incoherent.

297 The estimated phase difference is thus a random noise while the coherence  
 298 should be 0. If a target emerges from the sea surface, the signals received by

299 the antennas becomes coherent. High coherence values indicate the presence  
300 of scatterers and are used to further improve the detection and decrease the  
301 probability of false alarm. Only samples with coherence larger than 0.6 are  
302 considered to construct the binary image used for detection. The sensitivity  
303 of the method to the coherence threshold is presented in Appendix Appendix  
304 B.

305 Figure 6 presents an example of iceberg detection in SARin mode (Cy-  
306 cle 9 Pass 2772, 07/02/2015 22:10UT) near Greenland (see fig. 3). The  
307 waveforms, coherence and phase difference have been re-positioned using the  
308 L1 window delay and large and fine altitude instructions. The phase differ-  
309 ence is corrected for the pre-launch interferometric baseline of 0.612 radians  
310 (Bouzinac, 2012). Several icebergs are clearly visible in the MODIS image  
311 taken less than 45 min after the Cryosat pass (07/02/2015 20:10 UT). The  
312 signatures of 5 icebergs are clearly visible in the SARin waveforms between  
313  $64.1^\circ$  N and  $61.2^\circ$  N (Figure 6-a) and twenty-one CC's are detected. The co-  
314 herence presented in Figure 6-b confirms that icebergs are associated to very  
315 high coherence (between 0.71 and 0.99). The phase difference within CC's  
316 (Figure 6-c) strongly differs from the surrounding white noise and presents  
317 a high homogeneity. The CC characteristics as well as the iceberg area esti-  
318 mated using Equation 3 are presented in Table 2. As in the SAR example,  
319 the icebergs are associated to several (3 to 7) CC's corresponding to different  
320 elevations and/or portions of the icebergs. The across-track distance from  
321 nadir and free-board, computed using Equations 6 and 7 for each CC, are  
322 presented in Figure 6-d and -e. It should be noted that phase unwrapping  
323 is not necessary because the range of iceberg free-board ( $<100$  m) is small

324 enough to be fully covered by one phase rotation  $[-\pi + \pi]$ .

325 As for SAR mode, RDSAR waveforms can also be computed from SARin  
326 data. The RDSAR analysis (see Supplementary Information figure S1) de-  
327 tects only 2 icebergs (number 1 and 2) whose characteristics are given in  
328 Table 2. Iceberg 3 has a parabolic signature that overlaps the strong one of  
329 iceberg 2 and cannot be detected by the LRM algorithm. For icebergs 4 and  
330 5, no clear signatures were detected in RDSAR echoes mainly because the  
331 signatures are too close to the waveform leading edge where the noise level  
332 is larger in RDSAR.

333 The SARin detected signatures are irregularly spaced across-track and  
334 need to be re-sampled on a regular grid in order to geographically map the  
335 iceberg location, free-board and backscatter. The chosen grid is regular in  
336 the along- and across-track directions with an along-track resolution of 300  
337 m (i.e. the distance between two consecutive waveforms) and an across-track  
338 resolution of 50 m. The latitude and across-track distance of each CC pixel  
339 are remapped on the regular grid using classical earth's projections. The  
340 icebergs free-board is presented in Figure 6-d and their contours are plotted in  
341 Figure 6-g for comparison with MODIS data. The icebergs characteristics are  
342 then estimated by analyzing the CC and regions properties of the remapped  
343 free-board and backscatter fields. Table 2 presents the iceberg area estimated  
344 from the remapped SARin data as well as the areas estimated from the  
345 manually supervised analysis of the MODIS image of Figure 6-a and the  
346 Sentinel 1 SAR images (Wide swath mode of Figure B.4-a).

347 Icebergs 1 to 4, located between 0 and 3 km off-nadir, are very well de-  
348 tected and mapped compared to the MODIS and SAR images while the area

Table 2: Characteristics of the detected icebergs in Cryosat-2 SARin data on Pass 2772 Cycle 9, 07/02/2015 22:10 UT; and iceberg areas from the analysis of MODIS and Sentinel-1 images. RCS: radar cross section.

	SARin				SARin map		RDSAR			MODIS	Sentinel-1		
	lat	Range	Area	mean RCS	Max RCS	Area	Lat	Range	RCS	Area	Area	Area	
	deg	bin	pixel	km <sup>2</sup>	dB	dB	km <sup>2</sup>	deg	bin	dB	km <sup>2</sup>	km <sup>2</sup>	km <sup>2</sup>
1	64.204	128	216	1.0-2.0	-4.1	5.3	0.9	64.201	153	7.35	1.5	1.1-1.18	0.84
	64.204	172	15		-7.0	0.4							
	64.204	211	28		-4.8	5.0							
2	64.160	98	16	0.65-1.2	-15.0	-5.9	0.61	64.156	208	6.15	0.94	0.75-1.1	0.33
	64.160	133	49		-16.1	-9.5							
	64.160	181	32		-12.7	-7.7							
	64.160	208	45		-2.9	6.7							
3	64.138	80	9	1.0-2.1	-10.2	-5.4	0.55					0.6-1.1	0.29
	64.138	48	11		-14.3	-11.7							
	64.138	118	3		-15.8	-14.9							
	64.138	138	6		-15.4	-13.6							
	64.138	162	2		-18.7	-18.6							
	64.138	179	3		-14.2	-13.1							
4	64.127	177	38	0.4-0.8	-12.9	-9.9	0.43					0.4-0.8	0.21
	64.127	197	5		-11.4	-9.2							
	64.127	214	5		-10.2	-8.6							
5	64.103	196	9	0.2-0.4	-11.6	-10.3	0.13					0.8-1.2	1.16
	64.103	214	2		-9.6	-9.6							

349 of iceberg 5 located 5 km off-nadir, although detected, is largely underesti-  
 350 mated. This iceberg is located at the limit of the across-track range detection  
 351 window defined as a function of free-board elevation,  $\delta$ , and the time limits  
 352 of the noise range part of the waveform,  $t_0$  and  $t_1$ , by (Tournadre et al., 2008)

$$353 \quad \sqrt{(ct_0 + 2\delta)H''} \geq d_0 \geq \sqrt{(ct_1 + 2\delta)H''} \quad (8)$$

354 The comparison of the different area estimates given in Tables 2 SARin  
 355 remapped, RDSAR, MODIS and Sentinel-1, shows the very good agreement  
 356 of area estimates of the four eastern icebergs between SARin, RDSAR and  
 357 MODIS. The Sentinel-1 SAR are significantly lower by  $\sim 40\%$  In a recent  
 358 study comparing iceberg area estimate from SAR images and high resolution  
 359 visible images Mazur et al. (2017a) also found that an area error about 48%  
 360 for icebergs smaller than 0.5 km<sup>2</sup> and about 20% for icebergs between 0.5  
 361 and 1 km<sup>2</sup>. For the western iceberg, only partly detected, the area is under-  
 362 estimated by both RDSAR and SARin method. A confidence index for the  
 363 range limits of detection could be defined for each iceberg using Equation  
 364 A.1 as

$$365 \quad CI = \frac{d_0 - \sqrt{(ct_0 + 2\delta)H''}}{\sqrt{(ct_1 + 2\delta)H''} - \sqrt{(ct_0 + 2\delta)H''}} \quad (9)$$

366 CI should be between 0 and 1. The two area estimates of the RDSAR  
 367 detected iceberg are almost identical to the SARin ones. This validates the  
 368 simplified model used to infer area from range and backscatter.

369 Table 3 presents the area, mean and max free-boards and mean and max  
 370 backscatters of the five icebergs. The maximum backscatter for iceberg 1  
 371 is as in SAR mode case underestimated compared to the RDSAR, but for  
 372 iceberg 2 the maximum backscatter is larger in SARin mode than that in

Table 3: Iceberg characteristics from SARin analysis

iceberg number	1	2	3	4	5
Area (km <sup>2</sup> )	0.9	0.61	0.55	0.43	0.13
mean free-board (m)	26.1	22.8	36.5	20.6	27.9
max free-board (m)	36.3	38.9	49.1	25.6	29.5
mean backscatter (dB)	-7.1	-6.5	-13.5	-12.2	-11.9
max backscatter (dB)	3.8	4.5	-9.2	-8.8	-10.9

373 RDSAR. This might be related to the specularity of the echo.

374 The use of interferometry allows for the first time a direct estimate of  
375 the iceberg free-board. The mean iceberg free-board given in Table 3 ranges  
376 from 20.6 to 36.5 m while the maximum free-board ranges from 25.6 to  
377 49.1 m. Except for iceberg 3, the mean free-board is within a 20-30 m  
378 range, i.e. of the same order of magnitude as the 28 m free-board chosen  
379 as constant free-board for the RDSAR area estimate. The processing of  
380 the complete Cryosat-2 archive will allow to better estimate the free-board  
381 distribution for both Greenland and Southern Ocean icebergs and to improve  
382 the area-backscatter relationship. The mean free-boards are also well within  
383 the range of free-boards observed by ship radar in Eastern Greenland for  
384 large icebergs (<600 m length) presented by Dowdeswell et al. (1992). The  
385 across-track SARin resolution is high enough to allow the description of the  
386 iceberg complex topography as it can be seen in Figure 7 which presents  
387 the free-board for iceberg 1. Iceberg 1 is composed of a lower section whose  
388 elevation is about 18 m and a higher one about 30 m elevation with several  
389 spikes culminating at 40 m. Some of the spikes are associated with very high

390 backscatter while flatter surface are associated with low backscatter. The  
391 comparison with the coincident SAR and MODIS images (Figure 7-c and -d)  
392 shows not only a good agreement for the size of the iceberg but also for the  
393 backscatter distribution over the iceberg.

### 394 **3. Conclusion**

395 Cryosat-2 is the first altimeter to operate in three different modes over  
396 the ocean. Over most of the ocean it operates in the pulse limited LRM  
397 mode used by all past altimeters. The method of iceberg detection devel-  
398 oped by Tournadre et al. (2008) can be applied without modification and  
399 is currently used in the ALTIBERG small iceberg data base. The iceberg  
400 area is estimated from the iceberg backscatter and range using a backscat-  
401 ter model under hypotheses of constant free-board and ice backscatter. The  
402 LRM detection can also be applied to the pseudo-LRM or RDSAR waveforms  
403 computed from the SAR and SARin mode data. For Cryosat-2, RDSAR data  
404 are only available for a limited number of SAR and SARin orbits, but they are  
405 now part of the standard Sentinel-3 SAR data processing and both SAR and  
406 RDSAR are provided in Level 1 products. It will thus be possible to directly  
407 compare the detection and iceberg characteristics from both modes and thus  
408 to ensure the continuity and homogeneity between altimeters operating in  
409 different modes.

410 The stacking process used to compute SAR waveforms significantly re-  
411 duces the noise level of the waveform thermal noise part. This noise reduction  
412 facilitates the detection especially for smaller icebergs whose backscatter is  
413 too low to come out of RDSAR noise. The LRM parabolic signature of

414 icebergs reduces to bright spots in SAR data that can be easily detected  
415 using classical connected components and region properties algorithms. The  
416 iceberg area can be estimated using the along-track width and across-track  
417 length of the signature. However, as the across-track altimeter resolution  
418 strongly varies with the distance from nadir, only crude area estimates can  
419 be made and the RDSAR method based on range and backscatter appears  
420 more robust.

421 In SARin mode, both SAR and RDSAR echoes can be used to detect  
422 icebergs. Although the SNR is strongly reduced compared to SAR because  
423 of the reduction of the Burst mode Pulse Repetition Frequency (from 85.7 Hz  
424 to 21.4 Hz), the coherence can be used to improve the detection by limiting  
425 the probability of false alarm and by insuring the presence of a target above  
426 the sea surface. Furthermore, in this mode the range analysis window is four  
427 times larger than that in LRM and SAR mode. The number of range bins  
428 that can be used for detection is significantly larger, which almost double  
429 the detection swath of the altimeter from about 6 km to 12 km. The main  
430 interest of SARin mode is the possibility, for the first time for a satellite  
431 sensor, to precisely locate the surface scatterer and to allow the estimation  
432 of iceberg free-board and thus volume. The very high across-track accuracy  
433 also allows to map the iceberg topography at an unprecedented resolution.

434 Over the ocean where icebergs are more frequently present, i.e. near  
435 sea-ice covered regions, Cryosat-2 operates mainly in SAR mode. In the  
436 near future the SAR archive will be fully processed and included after inter-  
437 calibration with other altimeters in the ALTIBERG data set. The SARin  
438 mode is certainly the most powerful existing sensor to detect and characterize

439 small icebergs. Up to now only limited oceanic regions, around Greenland  
 440 or near Antarctica during Austral summers, are sampled in SARin mode.  
 441 However, the processing of the SARin archive will provide a unique iceberg  
 442 data-set that can be used to study the iceberg distributions of free-board,  
 443 size, area, length.

#### 444 **Appendix A. LRM detection**

445 The method of detection of iceberg using pulse limited altimeter data  
 446 was presented in detail by Tournadre et al. (2008) and is here briefly sum-  
 447 marized. An altimeter is a nadir looking radar that emits short pulses that  
 448 are backscattered by the sea surface. The altimeter measures the backscat-  
 449 tered power as a function of time to construct the echo waveform from which  
 450 the geophysical parameters are estimated. For Cryosat, the waveform range  
 451 analysis window is 128 bins of 3.125 ns (i.e. the compressed pulse length)  
 452 long or 60 m. A detailed description of the principles of the pulse limited  
 453 altimetry is given for example in Chelton et al. (2001). A point target of  
 454 height  $\delta$  above sea level located at distance  $d_0$  from the satellite nadir will  
 455 give an echo in the thermal noise part (i.e. above the mean sea surface) of  
 456 an altimeter waveform at the time  $t_i$  defined by (Powell et al., 1993)

$$457 \quad \frac{ct_i}{2} = -\delta + \frac{1}{2} \frac{R_E + H}{R_E H} d_0^2 = -\delta + \frac{d_0^2}{2H''} \quad (\text{A.1})$$

458 where  $c$  is the celerity of light,  $R_E$  the earth's radius,  $H$  the satellite  
 459 altitude, and  $H'' = H/(1 + H/R_E)$  is the reduced satellite height. In the  
 460 waveform space the signature of a point target is thus purely deterministic,  
 461 i.e. a parabola as a function of time when the satellite flies over the target. A

462 target is detectable if its echo time,  $t_i$  lies within the waveform range window  
 463 and if its backscatter coefficient is significantly larger than the thermal noise  
 464 of the sensor. The detection algorithm is based on the automated detection  
 465 of parabolas in the waveform noise part using the convolution product  $C$   
 466 between a filter,  $F$  characteristic of a target signature, and the thermal noise  
 467 part of the waveforms.

$$468 \quad C(k, l) = \sum_{n=1}^{N_1} \sum_{m=1}^{M_2} \sigma_0(k, l) F(k - n, l - m) \quad (\text{A.2})$$

469 where  $k$  is the telemetry sample index,  $N_1$ , the number of range bins used  
 470 for detection,  $l$ , the along-track waveform index, and  $\sigma_0$ , the echo power. For  
 471 each waveform of the detected parabola, the maximum of correlation  $C(l)$  and  
 472 its location  $k_{max}^C(l)$  (i.e. the range), and the maximum of backscatter,  $\sigma_{max}(l)$   
 473 and its location  $k_{max}^\sigma(l)$  are determined. A waveform is assumed to contain  
 474 an iceberg signature if  $C_{max}(l)$  and  $\sigma_{max}(l)$  are larger than given thresholds  
 475  $C_1$  and  $\sigma_1$  determined empirically by analysis of hundreds of signatures. The  
 476 iceberg range  $t_{ech}$  depends on the distance  $d$  from nadir of the iceberg center  
 477 and on the iceberg's free-board elevation  $h$  while its backscatter  $\sigma_{iceb}$  depends  
 478 on the area,  $A$ , the distance from nadir  $d$ , the backscattering coefficient of  
 479 the iceberg surface,  $\sigma_0^{ice}$ , which is conditioned by the ice characteristics, the  
 480 shape and roughness of the iceberg surface, and the presence of snow or water  
 481 on the iceberg surface.  $t_{ech}$  and  $\sigma_{iceb}$  are function of four main unknowns,  $d$ ,  
 482  $A$ ,  $h$  and  $\sigma_0^{ice}$ . The iceberg area can be estimated if assumptions are made  
 483 on the values of two of the remaining unknowns ( $d, h, \sigma_0^{ice}$ ).  $\sigma_0^{ice}$  is assumed  
 484 to be constant for all icebergs and set at 21 dB (Tournadre et al., 2012).  
 485 Following Gladstone et al. (2001) and Romanov et al. (2012) the free-board

486 elevation for icebergs larger than 200 m, is set at 28 m corresponding to a  
487 mean iceberg thickness of 250 m. Using these assumptions, the signature of  
488 square icebergs as a function of distance from nadir, (0 to 12 km), and area  
489 (0.01 to 9 km<sup>2</sup>) for each altimeter is computed using an analytic model of  
490 waveform. The range  $t_{ech} = f(d, A)$  and the mean backscatter  $\sigma_{iceb} = g(d, A)$   
491 are estimated from the modeled waveforms and used to compute an inverse  
492 model  $A = l(t_{ech}, \sigma_{iceb})$  and  $d = m(t_{ech}, \sigma_{iceb})$  for each altimeter.

## 493 **Appendix B. Sensitivity of the SAR and SARIn detection to the** 494 **power and coherence thresholds**

495 The SAR detection algorithm relies on the rms threshold used to binarize  
496 the normalized waveforms. The sensitivity of the method to this threshold  
497 has been tested using values from 3 to 6 rms (by 0.1 steps) for Cycle 9  
498 pass 2889. The results of the detection, area and backscatter estimate are  
499 presented in figure B.1. The threshold has no impact on the detection and  
500 none on the iceberg maximum backscatter. Low thresholds (<3.6) leads to  
501 an obvious overestimation of the area of the smallest iceberg (#3) estimated  
502 using equation 3. The underestimation of the mean backscatter for icebergs  
503 1 and 2 reflect the inclusion of water pixel in the signature. Thresholds from  
504 4 to 5 give very similar results for both area and backscatter with an rms  
505 smaller than 3% for area estimate and 2.8% for the mean backscatter. The  
506 threshold has been set to 4 rms.

507 The SARIn algorithm is similar to the SAR one and includes a second  
508 threshold on coherence in the waveform binarization. The rms threshold  
509 has been tested in the same way as previously with very similar results (not

510 presented here) for the Cycle 9 Pass 2772. For rms threshold above 3.5 there  
511 is almost no impact on the detection and parameter estimates. Coherence  
512 thresholds from 0.5 to 0.85 (by 0.1 steps) have been tested (using a rms  
513 threshold of 4) and the results are presented in figure B.2. Thresholds larger  
514 than 0.7 fail to detect iceberg 5 and those larger than 0.74 iceberg 3. For  
515 thresholds between 0.5 and 0.7, the rms of the area, mean freeboard and max  
516 backscatter are smaller than 18, 16 and 8 % respectively.

517 The area estimates were also compared to the ones manually obtained  
518 from the analysis of the 6 MODIS images (from Aqua and Terra satellites)  
519 (see figure B.3) and the 2 Sentinel 1 SAR images (Wide swath mode see figure  
520 B.4) available the same day as the Cryosat-2 pass. Iceberg 5 which lies at the  
521 limit of the Cryosat swath is not considered in the following. The resolution  
522 of the MODIS images (250 m) is similar to the along-track Cryosat resolution  
523 (300m) while the SAR images one (40m) is similar to Cryosat across-track  
524 one (50m). The MODIS estimates are quite scattered mainly because of  
525 the low resolution and of the impact of the solar angle and of the viewing  
526 incidence. However, there is an overall good agreement between the mean  
527 MODIS areas and the SARin ones for threshold between 0.55 and 0.65. The  
528 Sentinel 1 images presented in figure B.4 clearly show the presence of the  
529 5 icebergs. They are quite difficult to analyze because of the low contrast  
530 between ice and water for some part of the iceberg in both HH and HV  
531 polarizations. The SAR estimated areas are significantly lower (by ~40%)  
532 than the MODIS and SARin ones. Coherence around 0.7 would give results  
533 comparable to SAR images. However, we choose to set the threshold to 0.6  
534 as a trade-off between MODIS and SAR images estimates. In an operational

535 method the use of two thresholds can be used to give a first estimate of the  
536 method precision.

537 Sentinel-1 SAR images were provided by the European Space Agency.  
538 The study was partly funded by The French Centre National d'Etudes Spa-  
539 tiales. The MODIS data were provided by NASA. The ALTIBERG data set is  
540 available at the CERSAT web site: [http://cersat.ifremer.fr/user-community/news/item/473-](http://cersat.ifremer.fr/user-community/news/item/473-altiberg-a-database-for-small-icebergs)  
541 [altiberg-a-database-for-small-icebergs](http://cersat.ifremer.fr/user-community/news/item/473-altiberg-a-database-for-small-icebergs).

## 542 **References**

543 Bouzinac, C., 2012. Cryosat Product handbook. European Space Agency,  
544 ESRIN, Frascati, Italy.

545 Boy, F., Desjonquères, J. D., Picot, N., Moreau, T., Raynal, M., 2016.  
546 Cryosat-2 sar-mode over oceans: Processing methods, global assessment,  
547 and benefits. *IEEE Trans. Geoscienc. Rem. Sen.* PP (99), 1–11.

548 Chelton, D. E., Ries, J. C., Haines, B. J., Fu, L.-L., Callahan, P. S., 2001.  
549 Satellite Altimetry and Earth Science: A Handbook of Techniques and Ap-  
550 plications. Academic Press, San Diego, Ch. I: An Introduction to Satellite  
551 Altimetry, p. 463 pp.

552 Denbina, M., Collins, M. J., 2014. Iceberg detection using simulated dual-  
553 polarized radarsat constellation data. *Canadian J. Remote Sens.* 40 (3),  
554 165–178.

555 Depoorter, M. A., Bamber, J. L., Griggs, J. A., Lenaerts, J. T. M., Ligten-  
556 berg, S. R. M., van den Broeke, M. R., Moholdt, G., 2013. Calving fluxes  
557 and basal melt rates of Antarctic ice shelves. *Nature* 502.

- 558 Dinardo, S., 2013. Guidelines for the SAR (Delay-Doppler) L1b Processing.  
559 Tech. Rep. XCRY-GSEG-EOPS-TN-14-0042, European Space Agency,  
560 Frascati, Italy.
- 561 Dowdeswell, J. A., Whittington, R. J., Hodgkins, R., 1992. The sizes, fre-  
562 quencies, and freeboards of east greenland icebergs observed using ship  
563 radar and sextant. *J. Geophys. Res. : Oceans* 97 (C3), 3515–3528.
- 564 Enderlin, E. M., Howat, I. M., Jeong, S., Noh, M.-J., van Angelen, J. H.,  
565 van den Broeke, M. R., 2014. An improved mass budget for the greenland  
566 ice sheet. *Geophys. Res. Let.* 41 (3), 866–872.
- 567 ESA-ESTEC, 2007. CryoSat Mission and Data Description, CS-RP-ESA-SY-  
568 0059, Issue 3. European Space Agency, ESTEC, Noordwijk, The Nether-  
569 lands.
- 570 Galin, N., Wingham, D. J., Cullen, R., Fornari, M., Smith, W. H. F.,  
571 Abdalla, S., Jan 2013. Calibration of the Cryosat-2 interferometer and  
572 measurement of across-track ocean slope. *IEEE Trans. Geoscienc. Remote*  
573 *Sens.* 51 (1), 57–72.
- 574 Gill, R., 2001. Operational detection of sea ice edges and icebergs using sar.  
575 *Canadian J. Remote Sens.* 27 (5), 411–432.
- 576 Gladstone, R., Bigg, G., 2002. Satellite tracking of icebergs in the weddell  
577 sea. *Antarctic Science* 14, 278–287.
- 578 Gladstone, R. M., Bigg, G. R., Nicholls, K. W., 2001. Iceberg trajectory  
579 modeling and meltwater injection in the Southern Ocean. *J. Geophys. Res.*  
580 106, 19903–19916.

- 581 Gómez-Enri, J., Scozzari, A., Soldovieri, F., Coca, J., Vignudelli, S., 2016.  
582 Detection and characterization of ship targets using cryosat-2 altimeter  
583 waveforms. *Remote Sensing* 8 (3), 193.
- 584 Gommenginger, C., Martin-Puig, C., Amarouche, L., Raney, R. K., 2013.  
585 Review of state of knowledge for SAR altimetry over ocean. Tech. Rep.  
586 EUM/RSP/REP/14/749304, EUMETSAT, Darmstadt, Germany.
- 587 Green, C. L., Green, J. A. M., Bigg, G. R., 2011. Simulating the impact of  
588 freshwater inputs and deep-draft icebergs formed during a MIS 6 Barents  
589 Ice Sheet collapse. *Paleoceanography* 26 (2), A2211.
- 590 Hemming, S. R., 2004. Heinrich events: Massive late pleistocene detritus  
591 layers of the north Atlantic and their global climate imprint. *Rev. Geophys.*  
592 42, 1–43.
- 593 Jensen, J., Apr 1999. Angle measurement with a phase monopulse radar  
594 altimeter. *IEEE Trans. Antennas Propag.* 47 (4), 715–724.
- 595 Jongma, J. I., Driesschaert, E., Fichet, T., Goosse, H., Renssen, H., 2009.  
596 The effect of dynamic-thermodynamic icebergs on the Southern Ocean  
597 climate in a three-dimensional model. *Ocean Mod.* 26 (1-2), 104–113.
- 598 Marino, A., Dierking, W., Wesche, C., Sept 2016. A depolarization ratio  
599 anomaly detector to identify icebergs in sea ice using dual-polarization sar  
600 images. *IEEE Trans. Geoscienc. Rem. Sens.* 54 (9), 5602–5615.
- 601 Mazur, A., Wåhlin, A., Krezel, A., 2017a. An object-based SAR image ice-  
602 berg detection algorithm applied to the Amundsen Sea. *Rem. Sens. Envir.*  
603 189, 67 – 83.

- 604 Merino, N., Sommer, J. L., Durand, G., Jourdain, N. C., Madec, G., Mathiot,  
605 P., Tournadre, J., 2016. Antarctic icebergs melt over the southern ocean :  
606 Climatology and impact on sea ice. *Ocean Mod.* 104, 99–110.
- 607 Nanda, S., 2015. Multiple scatterer retracking and interferometric swath pro-  
608 cessing of CryoSat-2 data for ice sheet elevation changes. Master’s the-  
609 sis, Dpt. Geoscience & Remote Sensing, Fac. Civil Engineering and Geo-  
610 sciences, Technical University Delft, The Netherlands.
- 611 Powell, R. J., Birks, A. R., Wrench, W. J., Biddiscombe, C. L., 1993. Using  
612 transponders with ERS1-1 and Topex altimeters to measure orbit altitude  
613 to  $\pm 3$  cm. In: *Proc. First ERS- Symposium (ESA SP-359)*. pp. 511–516.
- 614 Raney, R., Sep 1998. The delay/Doppler radar altimeter. *IEEE Trans. Geo-*  
615 *scienc. Rem. Sens.* 36 (5), 1578–1588.
- 616 Ray, C., Martin-Puig, C., Clarizia, M. P., Ruffini, G., Dinardo, S., Gom-  
617 menginger, C., Benveniste, J., Feb 2015. SAR Altimeter backscattered  
618 waveform model. *IEEE Trans. Geoscienc. Rem. Sens.* 53 (2), 911–919.
- 619 Rignot, E., Jacobs, S., Mouginot, J., Scheuchl, B., 2013. Ice-shelf melting  
620 around Antarctica. *Science* 341, 266–270.
- 621 Romanov, Y., Romanova, N. A., Romanov, P., 2012. Shape and size of  
622 Antarctic icebergs derived from ship observation data. *Antarctic Science*  
623 24, 77–87.
- 624 Silva, T., Bigg, G., 2005. Computer-based identification and tracking of  
625 antarctic icebergs in sar images. *Remote Sens. Envir.* 94, 287–297.

- 626 Silva, T., Bigg, G., Nicholls, K., 2006. The contribution of giant icebergs to  
627 the Southern Ocean freshwater flux. *J. Geophys. Res.* 111, C03004.
- 628 Smal, I., Loog, M., Niessen, W., Meijering, E., Feb 2010. Quantitative com-  
629 parison of spot detection methods in fluorescence microscopy. *IEEE Trans.*  
630 *Med. Imag.* 29 (2), 282–301.
- 631 Smith, K. L., JUN 2011. Free-drifting icebergs in the Southern Ocean: An  
632 overview. *Deep Sea Res. Part II-Topical studies in Oceanography* 58 (11-  
633 12), 1277–1284.
- 634 Tournadre, J., Bouhier, N., Girard-Ardhuin, F., Remy, F., JAN 2016. Antarc-  
635 tic icebergs distributions 1992-2014. *J. Geophys. Res.* 121 (1), 327–349.
- 636 Tournadre, J., Girard-Ardhuin, F., Legresy, B., MAY 1 2012. Antarctic ice-  
637 bergs distributions, 2002-2010. *J. Geophys. Res.* 117, C05004.
- 638 Tournadre, J., Whitmer, K., Girard-Ardhuin, F., AUG 23 2008. Iceberg de-  
639 tection in open water by altimeter waveform analysis. *J. Geophys. Res.*  
640 113 (C8), C08040.
- 641 Wesche, C., Dierking, W., 2012. Iceberg signatures and detection in sar  
642 images in two test regions of the weddell sea, antarctica. *J. Glaciology*  
643 58 (208), 325–339.
- 644 Wingham, D., Francis, C., Baker, S., Bouzinac, C., Brockley, D., Cullen,  
645 R., de Chateau-Thierry, P., Laxon, S., Mallow, U., Mavrocordatos, C.,  
646 Phalippou, L., Ratier, G., Rey, L., Rostan, F., Viau, P., Wallis, D., 2006.  
647 CryoSat: A mission to determine the fluctuations in earth’s land and

648 marine ice fields. *Adv. Space Res.* 37 (4), 841–871, natural Hazards and  
649 Oceanographic Processes from Satellite Data.

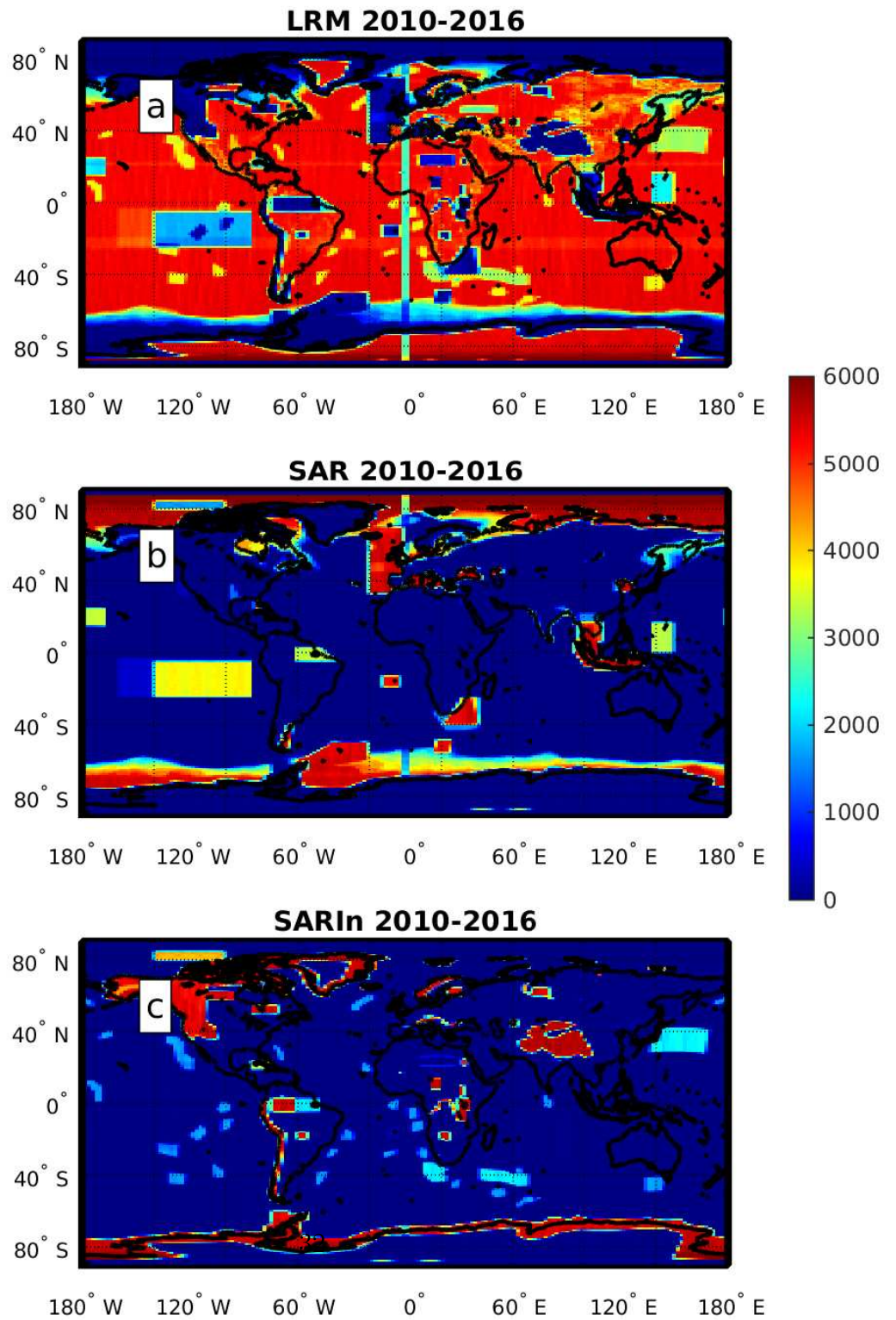


Figure 1: Number of Cryosat-2 measurements on a  $2^\circ \times 1^\circ$  latitude-longitude regular grid from 2010 to 2016. LRM mode (top), SAR mode (middle), SARin mode (bottom).

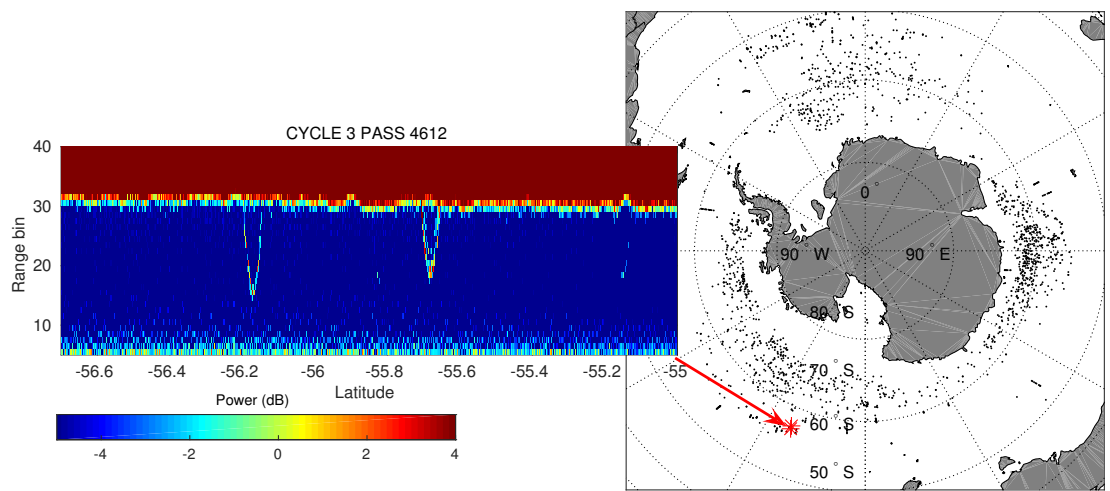


Figure 2: Icebergs detected using Cryosat-2 LRM data from 2010 to 2016 (black points). The left plot presents the signature of two icebergs detected in the South Pacific (red crosses) in the LRM waveforms (power in dB) of pass 4612 cycle 3.

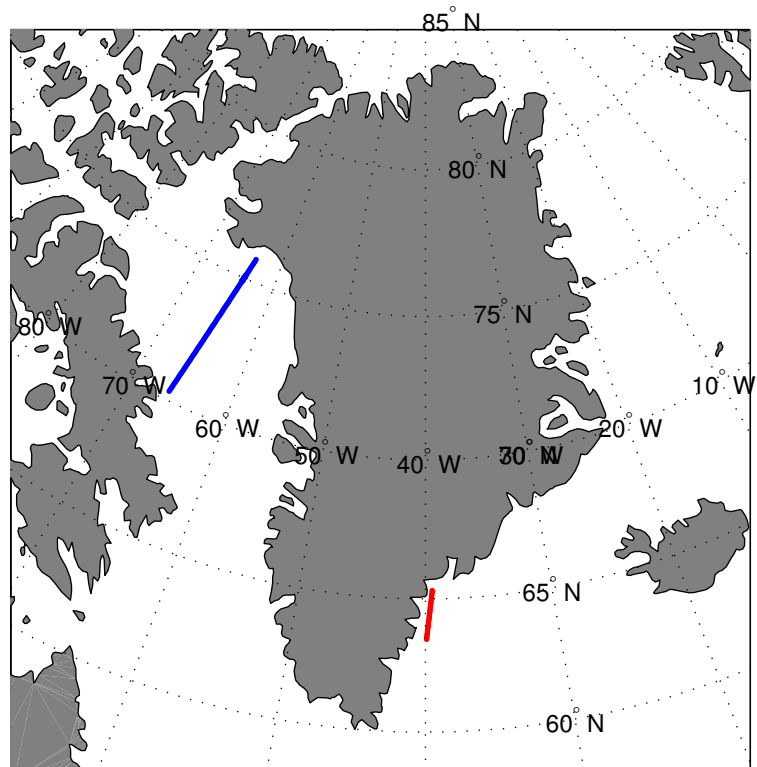


Figure 3: Location of the SAR (blue line) and SARin (red line) passes used for iceberg detection.

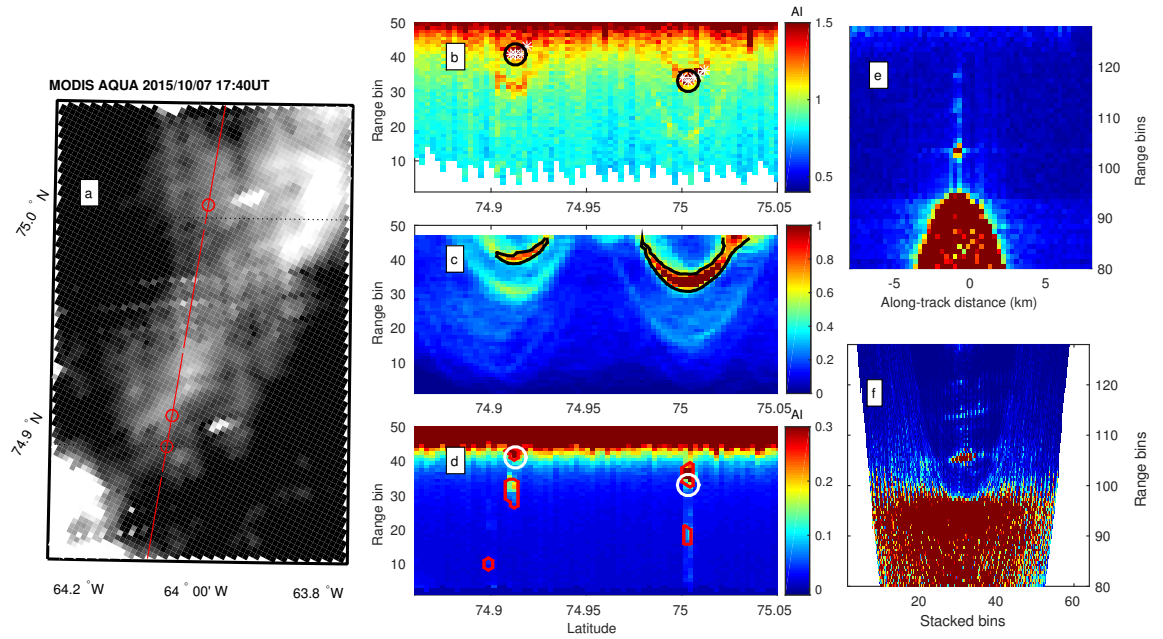


Figure 4: Example of detection of iceberg using SAR mode data (pass 2889 cycle 9, 2015/10/07 23:36 UT). (a) Aqua MODIS visible images at 250 m resolution on 2015/10/07 17:40 UT. The red line represents the altimeter ground track and the red circles the SAR detected icebergs. (b) Reduced SAR 20 Hz waveforms. The black circles indicate the detected icebergs and the white stars the position of the local echoes maximums. (c) Product of convolution between the filter and the RDSAR waveform used for detection, the black isoline represents the local maximums of correlation. (d) SAR 20 Hz waveforms. The red isolines show the SAR detected icebergs and the white circles the RDSAR ones. (e) Delay/Doppler map at 75° N. (f) Stacked Doppler beams at 75° N.

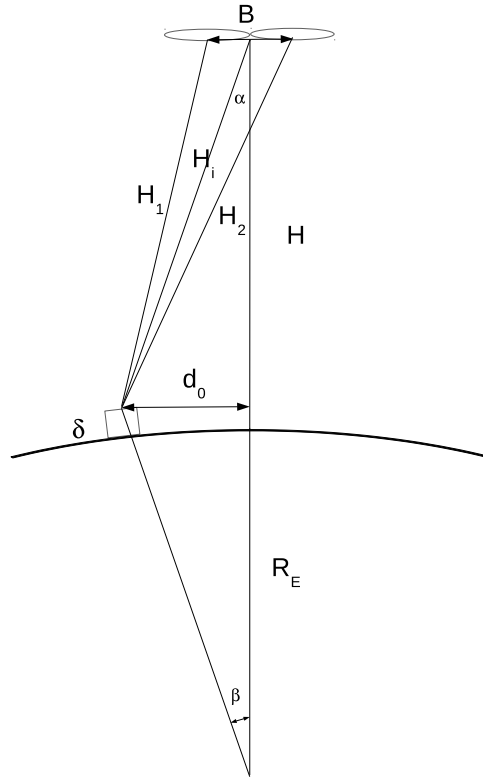


Figure 5: Cryosat-2 SARIn geometry.  $B$ : Baseline, i.e. distance between the two antennas,  $d_0$  distance of the iceberg from nadir,  $\delta$  iceberg's free-board,  $R_E$  earth's radius,  $H$  satellite altitude,  $H_1, H_2$  ranges of iceberg for the two antennas.  $\alpha$  off-nadir angle.

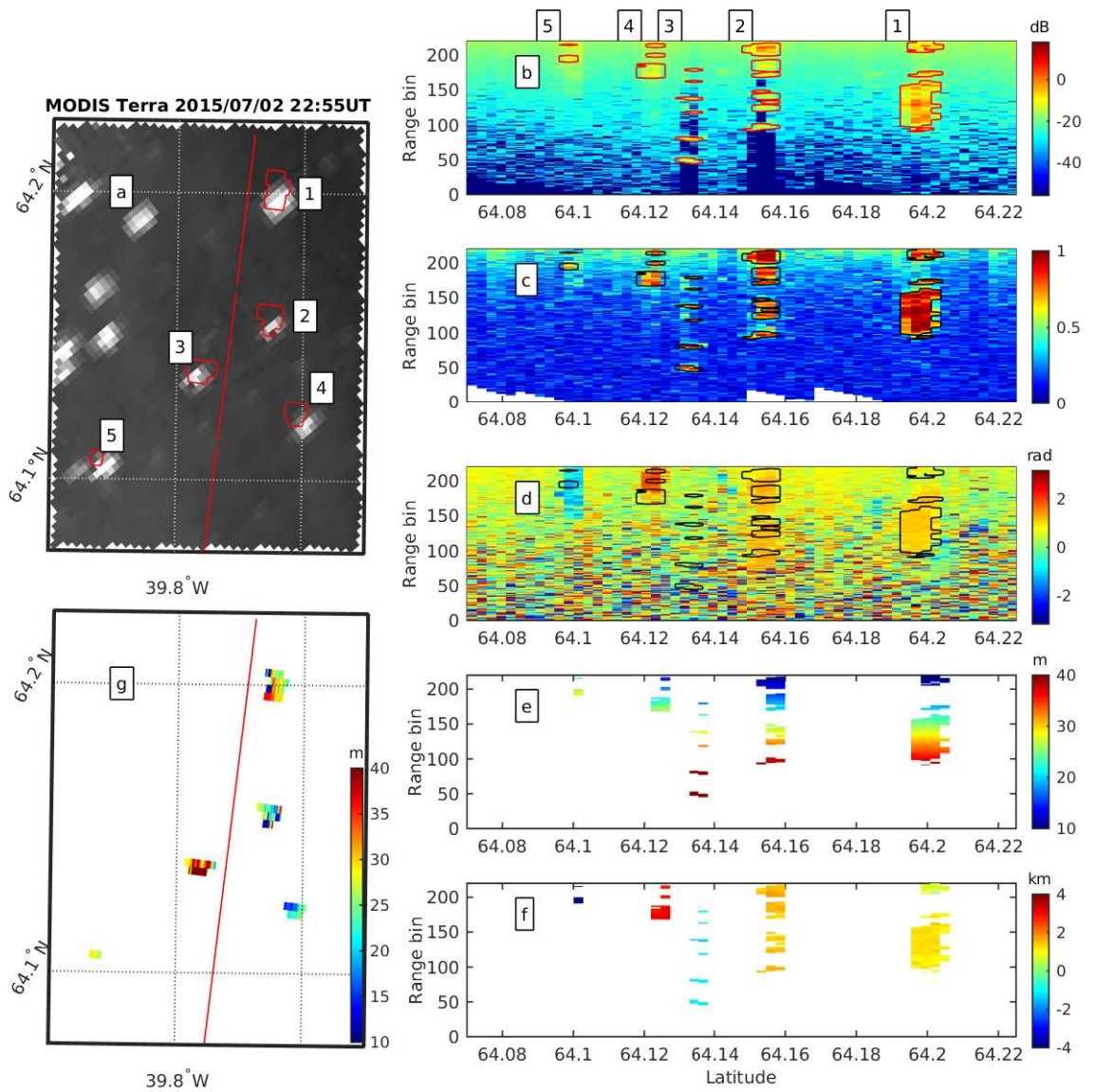


Figure 6: Iceberg detection using SARin data Cycle 9 Pass 2772, July 2nd 2015 22:10 UT. (a) MODIS Terra image on July 2nd 2015 22:55 UT. (b) SAR waveforms (in dB). (c) Interchannel coherence. (d) Phase difference (in rad). (e) free-board of the detected icebergs (in m). (g) Iceberg free-board remapped on a regular grid (in m). The red or black isolines represent the detected icebergs.

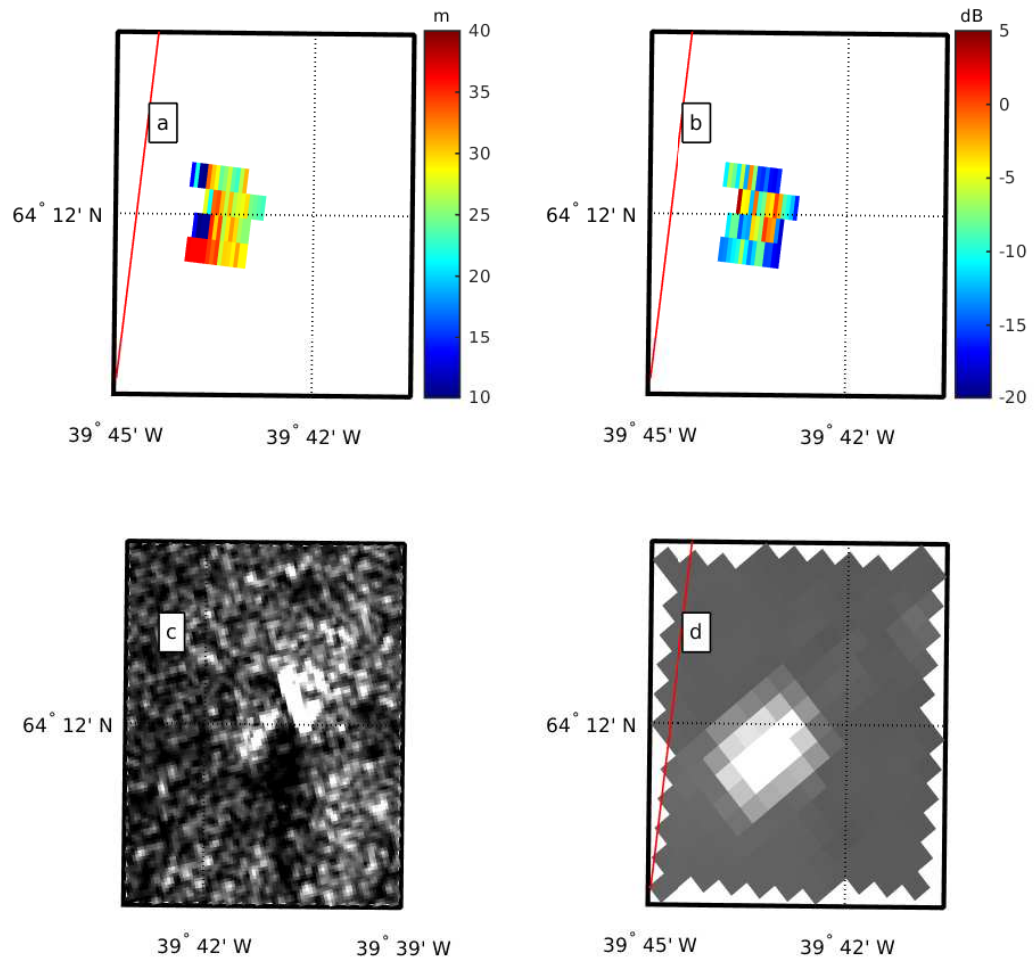


Figure 7: Detail of Iceberg 1 of Figure 6: (a) free-board (m). (b) Backscatter (dB) from Cryosat-2 on 07/02/2015 22:10UT. (c) Sentinel-1 SAR image on 07/01/2015 09:23 UT. (d) Detail of MODIS Terra image of figure 7-a (07/02/2015 22:55 UT).

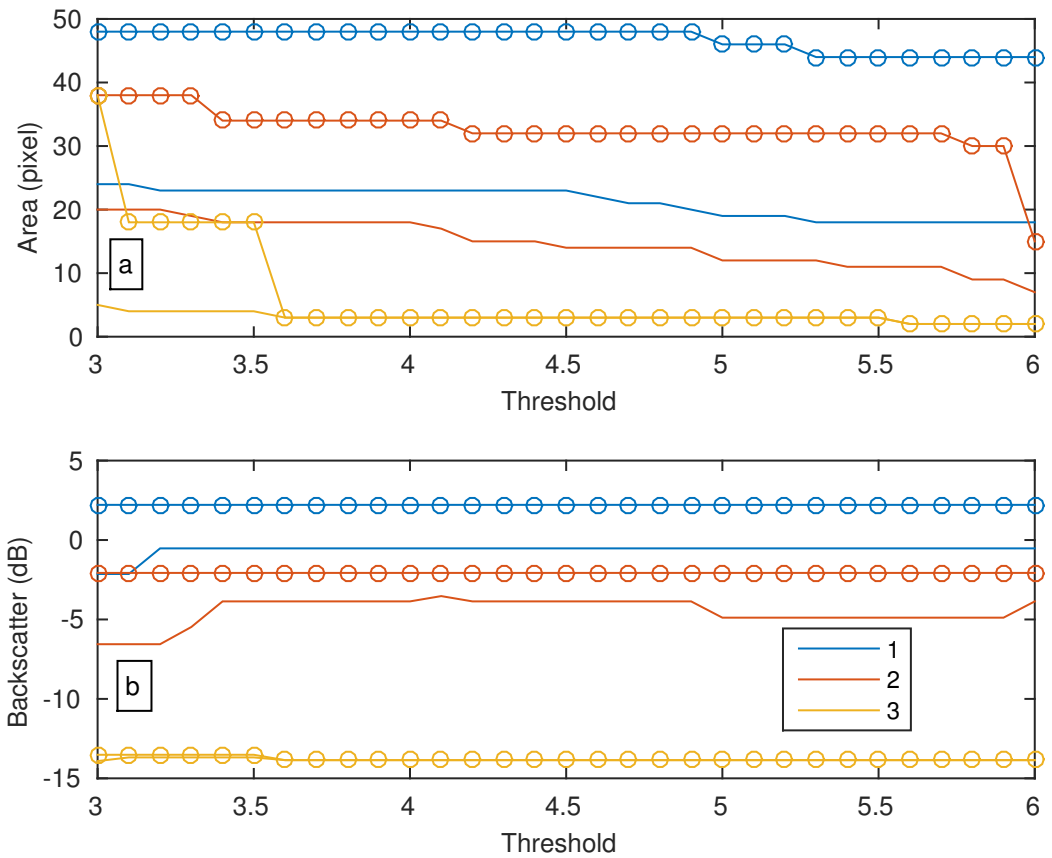


Figure B.1: (a) Iceberg signature areas using equations 2 (solid lines) and 3 (circles) as a function of rms threshold. (b) Mean (solid line) and maximum (circles) backscatter of the detected icebergs.

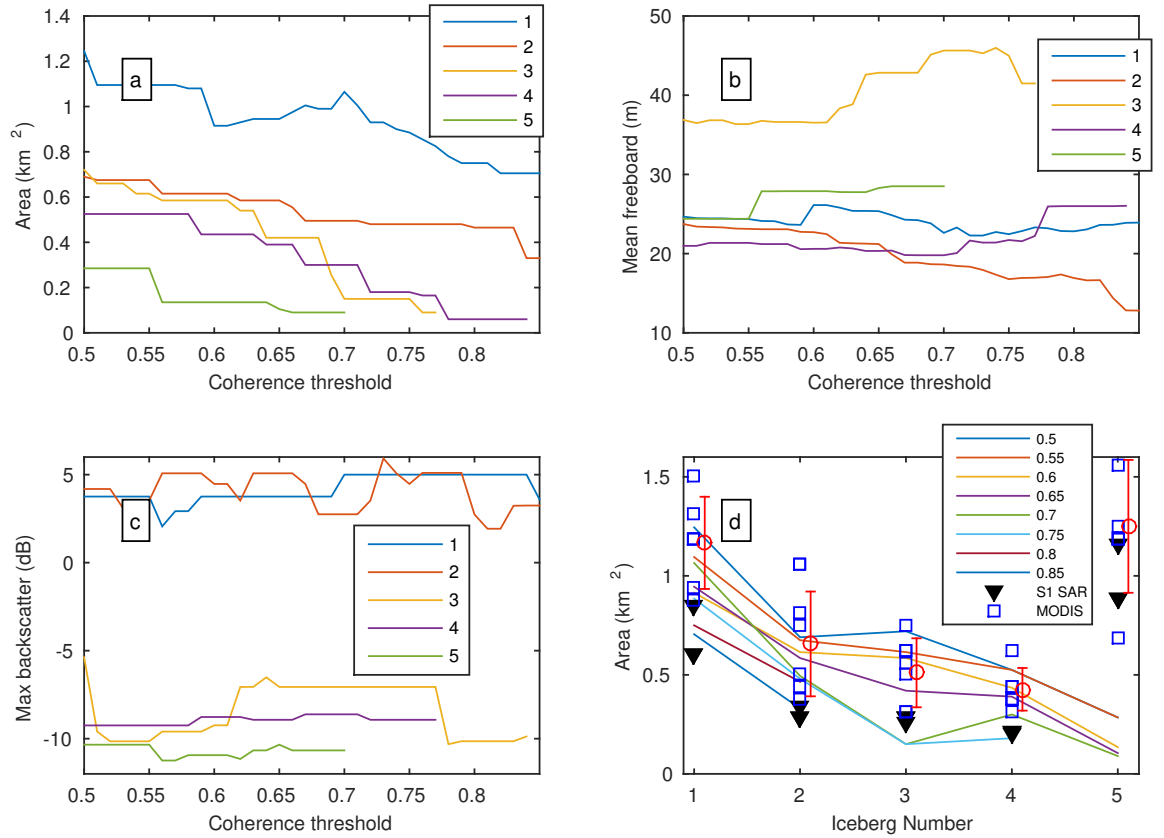


Figure B.2: (a) Area of the 5 icebergs of figure 7 as a function of the coherence threshold, (b) mean freeboard, (c) mean backscatter. (d) comparison of the SARin areas with Sentinel 1 (black triangle) and MODIS (blue square) images areas. The red error-bars represent the MODIS mean area and rms.

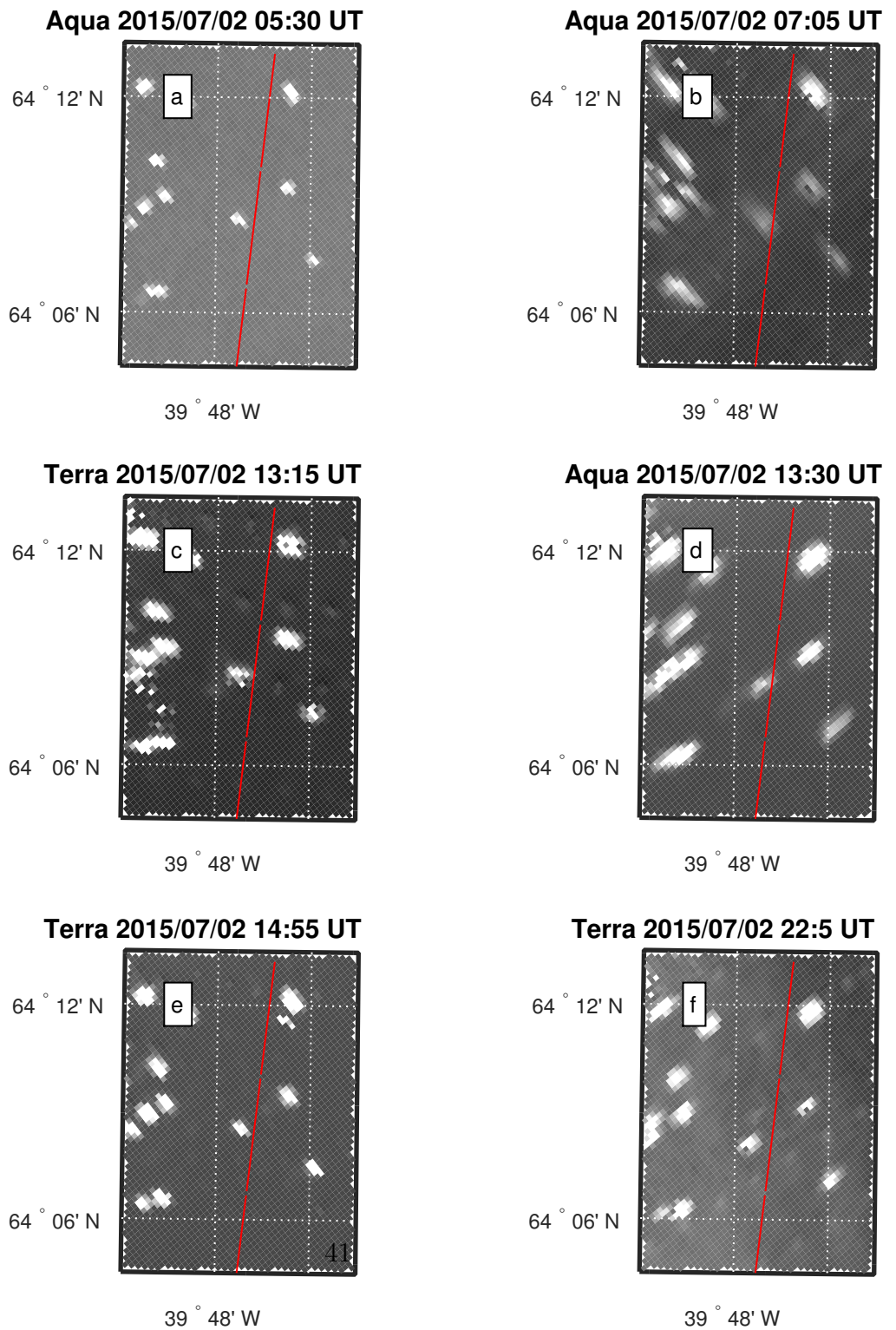
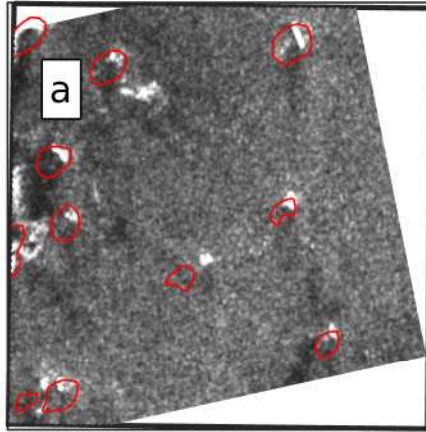
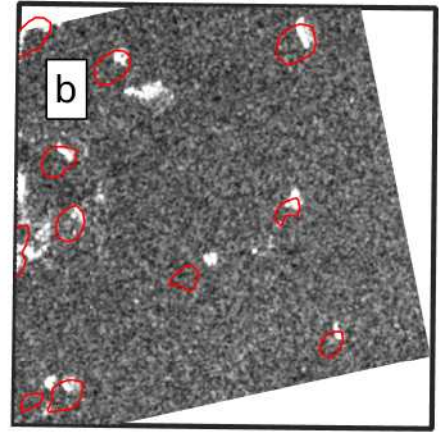


Figure B.3: MODIS images on July 2 2015. (a) Aqua 05:30 UT, (b) Aqua 07:05 UT, (c) Terra 13:15 UT, (d) Aqua 13:30 UT, (e) Terra 14:55 UT, (d) Terra 22:05 UT. The red lines represents the Cryosat-2 ground track of Cycle 9 Pass 2772

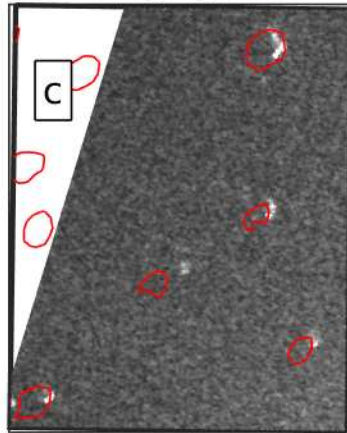
**S1A HH 2017/07/01 20:04 UT**



**S1A HV 2017/07/01 20:04 UT**



**S1A HH 2017/07/02 09:27 UT**



**S1A HV 2017/07/02 09:27 UT**

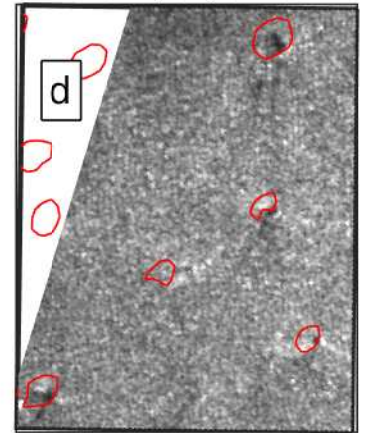


Figure B.4: Sentinel-1 wide Swath SAR images on July 1 and 2 2015. (a) HH and (b) HV polarization on July 1st 20:04 UT, (c) HH and (d) HV polarization on July 2nd 09:27 UT. The red lines represents the icebergs detected in the MODIS images presented in figure B.2-c and translated to take into account the movement of the group of iceberg.